ACS APPLIED MATERIALS & INTERFACES

www.acsami.org

Research Article

Self-Assembly of Shark Scale-Patterned Tunable Superhydrophobic/Antifouling Structures with Visual Color Response

Liang-Cheng Pan,[§] Shang-Yu Hsieh,[§] Wei-Cheng Chen, Fang-Tzu Lin, Chieh-Hsuan Lu, Ya-Lien Cheng, Hsiu-Wen Chien,* and Hongta Yang*

Cite This: *ACS Appl. Mater. Interfaces* 2023, 15, 35311−35320

Read Online

ACCESS | Metrics & More | Article Recommendations | Supporting Information

ABSTRACT: The stacked riblet-like shark scales, also known as dermal denticles, allow them to control the boundary layer flow over the skin and to reduce interactions with any biomaterial attached, which guide the design of antifouling coatings. Interestingly, shark scales are with a wide variation in geometry both across species and body locations, thereby displaying diversified antifouling capabilities. Inspired by the multifarious denticles, a stretchable shark scale-patterned silica hollow sphere colloidal crystal/polyperfluoroether acrylate-polyurethane acrylate composite film is engineered through a scalable self-assembly approach. Upon stretching, the patterned photonic crystals feature different short-term antibacterial and long-term anti-biofilm performances with a distinguished color response under varied elongation ratios. To gain a better understanding, the dependence of elongation ratio on antiwetting behaviors, antifouling performances, and structural color changes has also been investigated in this research.

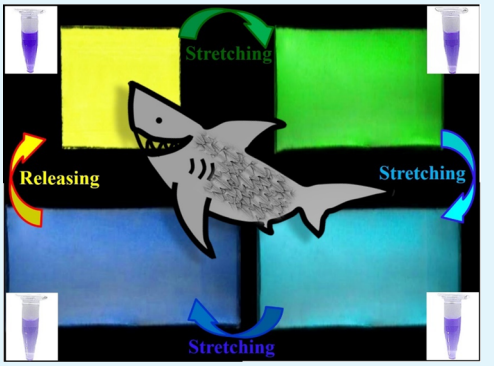

KEYWORDS: *shark scales, antifouling, self-assembly, photonic crystals, structural color*

INTRODUCTION

Biological fouling, commonly found on daily necessities, medical devices and supplies, underwater instruments, marine vessels, industrial equipment, etc., takes place as highly diverse bacteria, fungi, algae, or any other unwanted living organisms attach and grow onto the host surface where water is present.[1−4] Take industrial equipment as an example, the buildup of biofilm on membrane systems causes degradation to the primary purpose of that, while the colonization of micro- and macroorganisms in cooling water cycles or inside pipelines carrying oils with entrained water even poses considerable safety risks.[5−7] To address the issues, a great variety of antifouling strategies, including biocides, biodispersants, thermal treatments, ultrasonic cleaning, and pulsed laser/ultraviolet irradiation, are introduced to kill or prevent the organisms from settling.[8−12] Although biocides (e.g., tributyltin) and organic deposit dispersants have been widely utilized as antifouling agents, the chemical substances, unfortunately, suffer from extensive toxicity to marine living creatures. In contrast, the aforementioned energy methods provide a nonchemical, antifouling solution by denaturing or stunning the organisms with energizing of the water. However, the methodologies require an increased power source use and inevitably give rise to adverse environmental effects.

In recent years, a great deal of polymeric materials have been developed to serve as nontoxic antifouling coatings.[13−16] Ecologically inert fluoropolymers are the most common ones, which render low surface energies to prevent organisms from attaching and to facilitate the release of fouling organisms. Nevertheless, these hydrophobic surfaces are limited by low moduli of elasticity and poor mechanical strengths. In comparison with that, slippery surfaces with the use of highly hydrated zwitterions (e.g., sulfobetaine and glycine betaine) can remove water from attached organisms, thus deterring the organisms responsible for biofouling.[17,18] Unfortunately, the design and scalable synthesis of zwitterions remain problematic and the as-built coatings are not yet commercially available until very recently. Accordingly, there is an imperative need to develop environmentally friendly anti-biofouling materials.

Over more than 3.5 billion years of natural selection, living creatures have created diversified architectures to survive in diverse harsh environments. For instance, lotus (*Nelumbo nucifera*) leaves, prickly pear (*Opuntia*) skins, nasturtium (*Tropaeolum*) petals, bear cicada (*Cryptotympana takasagona* Kato) wings, and Formosan subterranean termite (*Coptotermes formosanus* Shiraki) wings are covered with waxy nano- and microstructures.[19−23] The low surface energy of wax allows air

Received: March 3, 2023
Accepted: June 27, 2023
Published: July 12, 2023

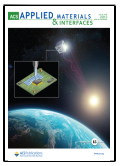

to be trapped between the hierarchical structures, bringing about increased surface hydrophobicities and enhanced self-cleaning properties. Nevertheless, the water-repellent architectures are short of preventing the formation of slimes and biofilms. The enlarged surface area, attributed to the increased surface roughness, makes it more favorable for bacterial colonization. Compared with these prototypes, some specific dolphin or shark skins, covered with riblet-like scales, show remarkable antifouling capabilities.[24,25] The inclined micrometer-scale structures not only offer poor anchor points for organisms but can also control boundary layer flows to release biofoulings. Bioinspired by the distinctive surface topologies, numerous shark scale-patterned coatings have been designed and built recently.[26−28] However, it remains a challenge to maintain their self-cleaning and antifouling performances either in stagnant water or without the presence of water. Moreover, shark skin-inspired materials with adjustable surface hydrophobicities and antifouling behaviors are rarely reported, even though they have been considered as a promising resolution to a wide range of technological applications, such as biomaterial separation membranes, tissue cultures, medical supplies, waste chemical recycling, etc.[29−31]

Benefiting from the rapid progress of polymer synthesis and nanofabrication technologies, polymer-based inverse opal photonic crystals have gained increasing attention to tackle incoming challenges. The flexible macroporous photonic crystals consisting of periodically arranged nanostructures possess an energy bandgap for the propagation of electromagnetic radiation with a particular frequency range.[32] Accordingly, the photonic surface exhibits a striking structural color, which is determined by the lattice spacing and effective refractive index of medium. Besides, the introduction of nanostructures generates an increased surface roughness. It is believed that the combination of inclined microstructures and nanostructures could make the surface less favorable for bacterial sorption, hence leading to extraordinary self-cleaning and anti-biofouling performances under varying environmental conditions.[33,34] Owing to the low Young's modulus values of polymeric materials, the patterned photonic crystals can be easily contorted under external mechanical stimuli. Their corresponding antifouling characteristics and optical properties are therefore adjustable through structure deformation. Unfortunately, most of the macroporous photonic crystals suffer from poor mechanical stability and durability, which considerably impede practical applications.[35]

To eliminate the issues, a number of robust and durable colloidal crystal/polymer composites have been developed and well-explored in the past decades.[36] The spontaneously crystallized colloidal crystals function as scaffolds to maintain temporarily deformed structures, accompanied by color changes, in response to external mechanical forces. In comparison with intricate and exorbitant lithography-based technologies, the colloidal self-assembly methodologies render a relatively simple and inexpensive strategy to fabricate photonic crystals. However, the bottom-up approaches, including gravitational sedimentation, capillary-force-induced assembly, physical confinement, electric/magnetic-field-assisted assembly, etc., are limited by time-consuming and laboratory-scale productions.[37−40] Apart from that, the small refractive index differences between commonly used colloids and polymers generate low color saturation performances and only allow translucent appearances. Facile and large-scale fabrication of photonic crystals with reversible mechanochromic responses thereupon remains an unmet yet urgent need.

Herein, a roll-to-roll compatible doctor-blade-coating technology is developed to assemble hollow sphere colloidal crystal/polymer composites onto a shark scale-patterned negative replica. Thanks to its high-throughput coating speed, a wide range of coating materials, and low coating material wastage, the coating technology is even suitable for industrial-scale mass production. Importantly, the elastic polymer matrix allows mechanical deformation and shape recovery under ambient conditions. In consequence, tunable surface morphology and characteristics of the as-engineered shark scale-patterned photonic crystals can be achieved by applying external mechanical stimuli. The corresponding structural color is therefore real-time altered under varied elongation ratios, realizing perceivable monitoring by readable optical signals.

EXPERIMENTAL SECTION

Materials. A male shortfin mako shark specimen, reaching 120 cm in length, is obtained from Pacific waters around Taiwan. Glutaraldehyde aqueous solution (25%) and ethanol (95%) are purchased from Merck. Sylgard 184 poly(dimethylsiloxane) (PDMS) precursors containing base and curing agents are supplied by Dow Corning. The chemicals and solvents applied to synthesize silica hollow spheres, including styrene monomers (99%), potassium persulfate (≥99%), sodium dodecyl sulfate (≥95%), anhydrous ethanol (200 proof), ammonium hydroxide (28−30%), and tetraethyl orthosilicate (98%), are provided by Thermo Fisher Scientific. Deionized water (18.2 MΩ cm) purified in a Milli-Q IQ 7003 ultrapure water system is directly used in the experiments. Commercial UV-curable perfluoroether acrylate (PFA, UV-T) oligomers and UV-curable urethane acrylate (UA, ETERANE 8928) oligomers are acquired from Exfluor and Eternal Materials, respectively. The photoinitiator, 2-hydroxy-2-methyl-1-phenyl-1-propanone (Darocur 1173), is provided by BASF. Gram-negative *Escherichia coli* (*E. coli*, ATCC 23501), employed as a model strain, is obtained from the Food Industry Research and Development Institute in Taiwan. The bacterial suspension buffer is acquired from Gold Biotechnology. Commercial lactate dehydrogenase (LDH) kit, including Triton X-100 (97%), phosphate-buffered saline (PBS, pH 7.4), sodium L-lactate (≥99%), β-nicotinamide adenine dinucleotide hydrate (β-NAD), diaphorase, bovine serum albumin (BSA, 98%), sucrose (≥99%), 2-(4-iodophenyl)-3-(4-nitrophenyl)-5-phenyltetrazolium chloride (INT, 98%), and sodium oxamate, is supplied by Thermo Fisher Scientific. Tryptic soy broth (TSB), used as culture media to support the growth of *E. coli*, is supplied by Cyrusbioscience. The chemicals used to evaluate long-term antifouling properties, including glucose, crystal violet (CV, 1%), and methanol (≥99%), are provided by Thermo Fisher Scientific and Merck, respectively. All of the chemicals are of reagent quality and are used as received.

Instrumentation. Scanning electron microscopy is performed on a JEOL JSM-7800F field emission scanning electron microscope and a JEOL JSM-6335F field emission scanning electron microscope. The specimens are coated with platinum by a Ted Pella Cressington 108 auto sputter coater prior to imaging the surface morphologies. Optical reflection spectra in the wavelength range from 300 to 700 nm are collected using an Ocean Optics HR4000 ultraviolet−visible−near-infrared spectrometer with an Ocean Optics DT-MINI-2 light source. Uniaxial tensile tests and cyclic tensile tests are carried out using a Shimadzu Autograph AGS-X series universal testing machine. Water contact angles are gauged using a KRÜSS DSA100 drop-shape analyzer with a droplet volume of 10 μL under ambient conditions. The average of 10 measurements on different regions of each specimen is reported. To evaluate short-term/long-term bacterial attachments, the absorbances are measured spectrophotometrically at 490 and 590 nm, respectively, using a BMG LABTECH SPECTRO

https://doi.org/10.1021/acsami.3c03086
ACS Appl. Mater. Interfaces 2023, 15, 35311−35320

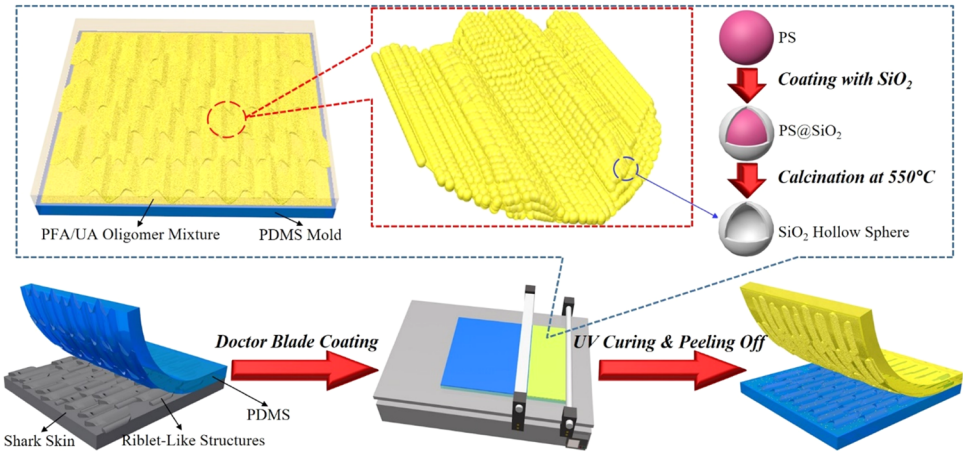

Figure 1. Experimental procedures for assembling photonic crystal-based superhydrophobic/antifouling structures using a doctor-blade-coating technology.

star Nano microtiter plate reader. Optical density (OD) is served as a rapid proxy measurement of the number of adherent bacteria.

Pretreatment of Shark Skins. Fresh shark skins are collected from the flank region of shortfin mako shark, the dermal and subcutaneous tissues of which are detached using a razor blade. After rinsing with deionized water to eliminate any biological residue on scales, the shark skins are sandwiched between glass slides and immersed in an aqueous glutaraldehyde solution (2.5%) for 6 h to maintain their shapes. Afterward, the skins are dehydrated through successive ethanol washes (30, 50, 70, 85, 90, 95, and 100%) for 1 h each, and then are air-dried at 37 °C for 12 h.

Fabrication of PDMS-Negative Replicas. The shark scale patterns are replicated through conventional soft lithography using PDMS. A mixture of PDMS precursors containing base/curing agents at a weight ratio of 10:1 is degassed and then poured onto the shark skin specimen. After being cured at 65 °C overnight, the solidified PDMS-negative replica can be gently peeled off from the specimen.

Preparation of UV-Curable Silica Hollow Sphere Dispersions. The aqueous emulsion polymerization of styrene monomers is carried out in the presence of potassium persulfate as an initiator and sodium dodecyl sulfate used as an anionic surfactant under nitrogen atmosphere at 85 °C for 12 h.[41] During the polymerization process, negatively charged emulsions electrostatically repel each other to maintain their monodispersity in size. The as-synthesized polystyrene spheres are rinsed with anhydrous alcohol to eliminate any residual chemical and then serve as sacrificial templates to develop silica hollow spheres with controllable size and shell thickness.[42,43] For the hard-template synthesis strategy, polystyrene spheres are dispersed in a mixture of anhydrous alcohol, deionized water, and ammonium hydroxide, followed by swiftly injecting tetraethyl orthosilicate into the mixture under vigorously stirring at 50 °C. In the sol−gel process, the hydrolysates of tetraethyl orthosilicate are coupled to form silica particulates on the polystyrene spheres. The stacked silica particulates gradually transform into a uniform and smooth shell with the increase of reaction period, while the surface morphology and shell thickness are not significantly changed after 12 h. The as-fabricated polystyrene-core/silica-shell spheres are cleansed with anhydrous alcohol in 5 centrifugation and dispersion cycles and then calcined at 560 °C for 6 h to completely remove the polystyrene cores. The resultant silica hollow spheres are collected and redispersed in an oligomer mixture containing UV-curable PFA oligomers, UV-curable UA oligomers, and 2-hydroxy-2-methyl-1-phenyl-1-propanone using a Thermolyne vortex mixer.

Self-Assembly of Shark Scale-Patterned Composite Films with Colloidal Crystals Embedded. The as-prepared silica hollow sphere dispersion is doctor-blade-coated onto the PDMS-negative replica at a coating speed of 5 mm/s using an Elcometer 4340 automatic film applicator, during which the blade offers a unidirectional shear force to assemble the silica hollow spheres. The oligomers are then photopolymerized under UV radiation in a drawer-type OPAS XLite-500 UV curing chamber. On account of the low elastic modulus and low surface energy of PDMS, the negative replica can be easily deformed. After peeling off the PDMS mold, a shark scale pattern-covered composite film with silica hollow sphere colloidal crystals embedded is produced.

Tensile Tests. For the uniaxial tensile testing, dumbbell-shaped specimens with the standard ASTM D412 size (100 mm (length) × 3 mm (width) × 3 mm (thickness)) are cut by a punch and examined with a crosshead speed of 10 mm/min and an initial grip separation of 25 mm. Young's moduli of the specimens are calculated to be the slopes of initial linear regions (strain <50%) of the tensile curves. For the cyclic loading−unloading tensile testing, dumbbell-shaped specimens are stretched to on-demand strains (10, 20, 30, 40, and 50%) and then retracted back to their initial lengths at a constant speed of 10 mm/min. The tensile tests of all of the specimens are performed under ambient conditions.

Analysis of Antifouling Properties. The antifouling performance is investigated through evaluating short-term/long-term bacterial attachments on the specimens. *Escherichia coli* (*E. coli*) are suspended in a sterilized saline solution (0.85%) at neutral pH, in which the concentration of bacteria is adjusted to be ~1×10^9 CFU/mL. In the short-term bacterial attachment assessment, the bacterial suspension is deposited onto the specimens and then incubated at 37 °C for 24 h. Afterward, the specimens are rinsed with sterilized saline to eradicate any unattached bacteria, while the attached ones are lysed by Triton X-100 (0.5%) at 37 °C for half an hour. Each of the bacterial lysates is mixed with a PBS solution containing sodium L-lactate (12 mg/mL), β-NAD (1 mg/mL), diaphorase (0.9 mg/mL), BSA (0.1%), sucrose (4 mg/mL), and INT (0.067 mg/mL), where the volume ratio of the lysate to the PBS solution is controlled to be 1:1. The mixture is then incubated at 37 °C for another 1 h to gradually release LDH from the lysates. After terminating the reaction by applying a sodium oxamate solution (16 mg/mL), the LDH present in the resulting mixture is measured using a microtiter plate reader to determine the number of adherent bacteria. For the long-term biofilm formation assessment, a bacterial suspension (1×10^9 CFU/mL) containing glucose (1%) is deposited onto the specimens and then incubated at 37 °C at a shaking frequency of 85 rpm for 10 days. During the inoculation, the culture medium is refreshed with TSB (1% glucose) every 2 days. After rinsing with sterilized saline, the adherent biofilms are stained with CV and solubilized in methanol for evaluating long-term attachment of bacteria using a microtiter plate reader.

RESULTS AND DISCUSSION

The experimental procedures for engineering shark scale-patterned composite films with photonic crystals embedded are schematically illustrated in Figure 1. Dehydrated shortfin

https://doi.org/10.1021/acsami.3c03086
ACS Appl. Mater. Interfaces 2023, 15, 35311−35320

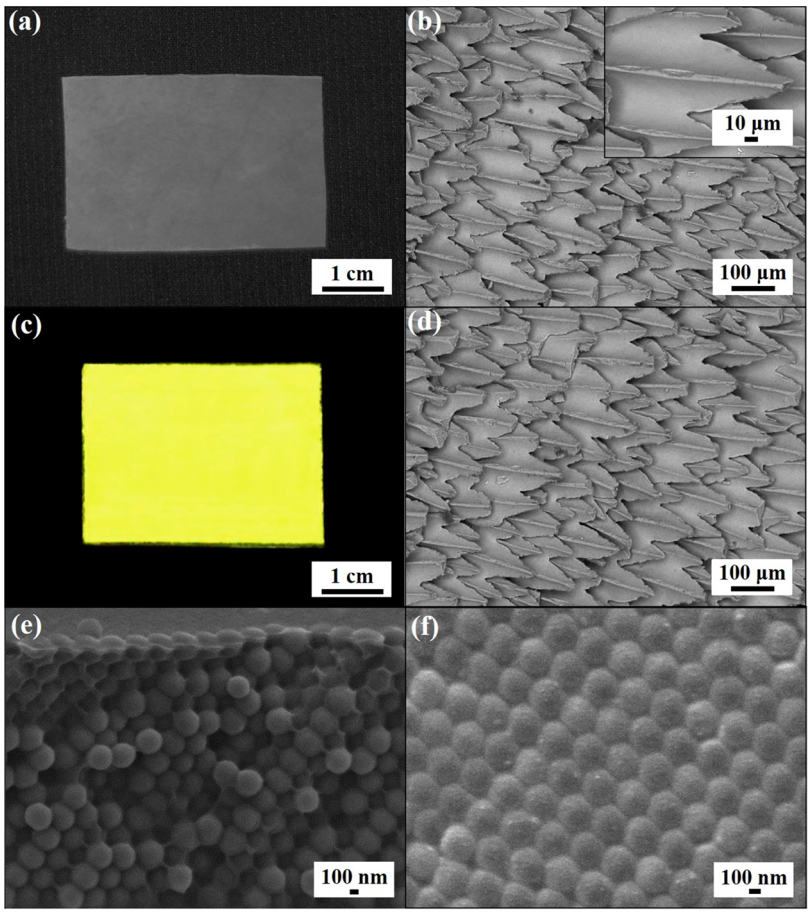

Figure 2. (a) Photographic image of a piece of shortfin mako shark (*Isurus oxyrinchus*) skin. (b) Top-view SEM image of the specimen in (a); the inset displays a higher-magnification SEM image. (c) Photographic image of a templated riblet-like structure-covered composite film with 280 nm hollow sphere colloidal crystals embedded. The image is taken from the shark scale pattern-covered side of the specimen. (d) Top-view SEM image, (e) magnified cross-sectional SEM image, and (f) magnified top-view SEM image of the specimen in (c).

mako shark skin specimens are utilized as templates to fabricate PDMS-negative replicas. The negative replica can be doctor-blade-coated with a silica dispersion, consisting of silica hollow spheres, UV-curable PFA oligomers, UV-curable UA oligomers, and 2-hydroxy-2-methyl-1-phenyl-1-propanone as a photoinitiator. In the dispersion, the volume ratios of silica hollow spheres, PFA oligomers, UA oligomers, and the photoinitiator are controlled to be 74:8:17:1. The monodisperse silica hollow spheres, templated from 234 nm polystyrene cores, are with an average diameter of 280 nm and an average wall thickness of 23 nm (Figure S1). In the coating process, the blade renders a unidirectional shear force for aligning the suspended silica hollow spheres. The shear-thinning behavior of the silica dispersion results in the formation of close-packed silica hollow sphere colloidal crystals. It is worth mentioning that the thickness of doctor-blade-coated colloidal crystals can be determined through adjusting the coating speed, the gap size, and the rheological properties of dispersion.[44] After polymerization of the oligomers under UV radiation, a shark scale pattern-covered silica hollow sphere colloidal crystal/polymer composite film can be easily peeled off from the PDMS-negative replica.

Figure 2a shows a photographic image of a dehydrated shark skin specimen. Although distinct lumps or indentations are not recognized by the naked eye, the skin is covered with highly ordered transparent placoid scales (Figure 2b). The stacked micrometer-scale riblet-like scales can be templated into a flexible PDMS-negative replica (Figure S2), which is then employed as a second-generation template to pattern the structures onto a doctor-blade-coated composite film with 280 nm hollow sphere colloidal crystals embedded. The intrinsic low surface energy of PDMS facilitates the replication of riblet-shaped patterns without any surface modification. In contrast to the appearance of shark skin, the as-templated riblet-like structure-covered composite film exhibits a uniform yellow color under white light illumination (Figure 2c,d). The structural color is attributed to Bragg diffraction of visible light from the three-dimensionally hexagonal close-packed silica hollow spheres, which are surrounded by a PPFA-PUA matrix (Figure 2e,f). It is worth noting that the diffraction peak position of the crystalline structures can be correlated to the effective refractive index (n) of the medium and the interlayer lattice spacing (d) using Bragg's equation[45]

$$\lambda_{peak} = 2 \times (f_{air} \times n_{air}^2 + f_{silica} \times n_{silica}^2 + f_{PPFA\text{-}PUA} \times n_{PPFA\text{-}PUA}^2)^{1/2} \times d \times \sin 90^\circ$$

where f_{air} (0.43), n_{air} (1), f_{silica} (0.31), n_{silica} (1.42), $f_{PPFA\text{-}PUA}$ (0.26), and $n_{PPFA\text{-}PUA}$ (1.48) represent the volume fractions and refractive indices of air, silica, and polymer, respectively. The estimated peak position (581 nm) locates within a wavelength range of 570−590 nm, the yellow region of the visible spectrum. Moreover, in comparison with the refractive

https://doi.org/10.1021/acsami.3c03086
ACS Appl. Mater. Interfaces 2023, 15, 35311−35320

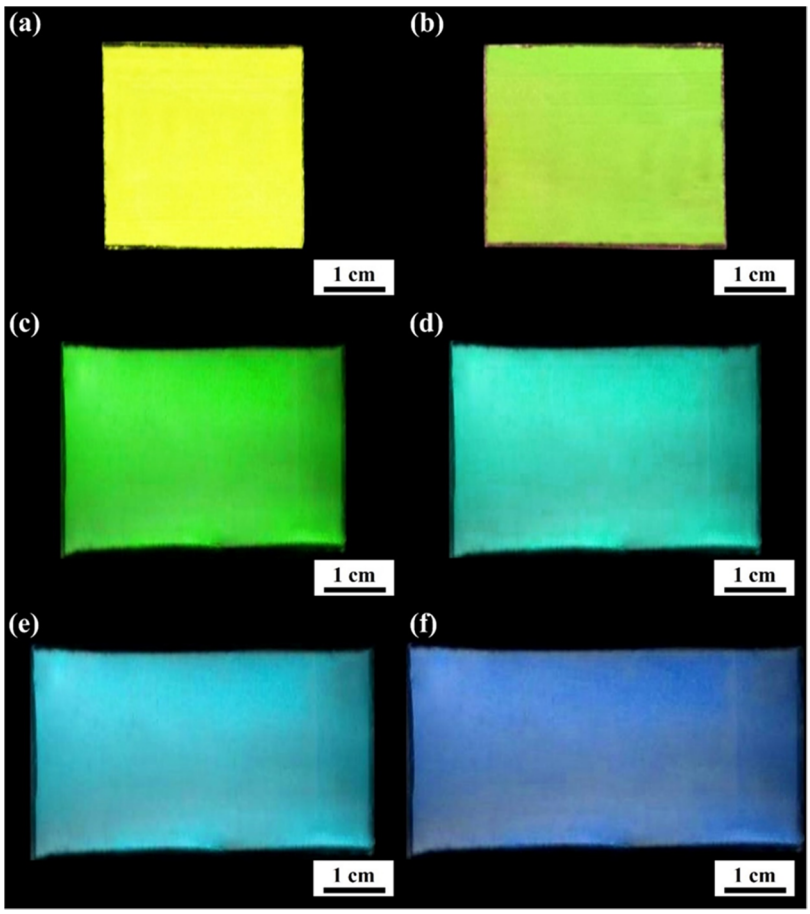

Figure 3. Photographic images of a templated riblet-like structure-covered composite film with 280 nm hollow sphere colloidal crystals embedded under varied elongation ratios. (a) Unstretched state; (b) elongation ratio = 0.1; (c) elongation ratio = 0.2; (d) elongation ratio = 0.3; (e) elongation ratio = 0.4; (f) elongation ratio = 0.5. The images are taken from the shark scale pattern-covered sides of the specimens.

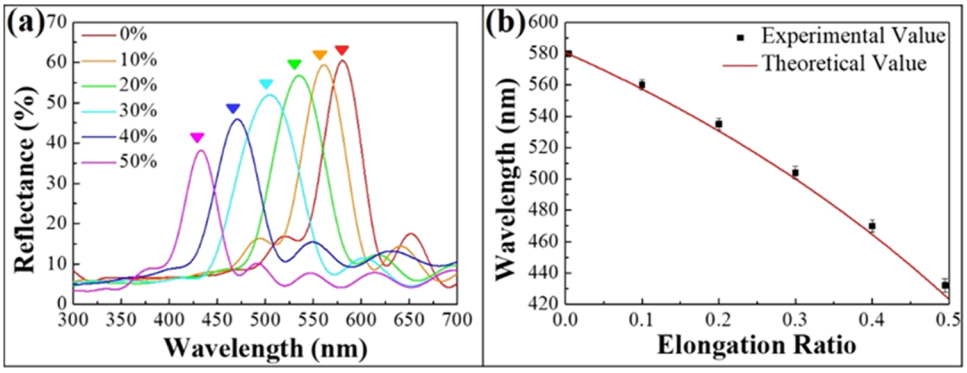

Figure 4. (a) Normal-incidence spectral reflection spectra of a templated riblet-like structure-covered composite film with 280 nm hollow sphere colloidal crystals embedded under varied elongation ratios from 0 (red curve) to 0.5 (pink curve). The arrows denote the corresponding reflection peak positions estimated by Bragg's law. (b) Dependence of the optical reflection peak position on elongation ratio.

index difference between n_{Silica} (1.42) and n_{Polymer} (~1.45), a larger one between the $n_{\text{Silica Hollow Sphere}}$ (1.14) and the $n_{\text{PPFA-PUA}}$ (1.48) leads to a higher reflection intensity.[46] As a result, the composite film displays a brilliant yellow color with high color saturation. The reflection intensity can be even enhanced through increasing the thickness of colloidal crystals.

Importantly, the PPFA-PUA matrix is with high elasticity and can be temporarily deformed upon applying a force within its elastic limit.[47] Owing to that, the elastic deformation of silica hollow sphere colloidal crystal/PPFA-PUA composite film under longitudinal stretching allows the embedded silica colloidal crystals to create a reduced interlayer lattice spacing (d) (Figure S3), and hence brings about a blue shift of the resulting bandgap position. The corresponding structural color therefore shifts from yellow (unstretched state), chartreuse (elongation ratio = 0.1), green (elongation ratio = 0.2), cyan (elongation ratio = 0.3), and blue (elongation ratio = 0.4) to violet (elongation ratio = 0.5) under varied elongation ratios (Figure 3). Noteworthily, the composite film can temporarily maintain the stretched structures without applying any contact

https://doi.org/10.1021/acsami.3c03086
ACS Appl. Mater. Interfaces 2023, 15, 35311−35320

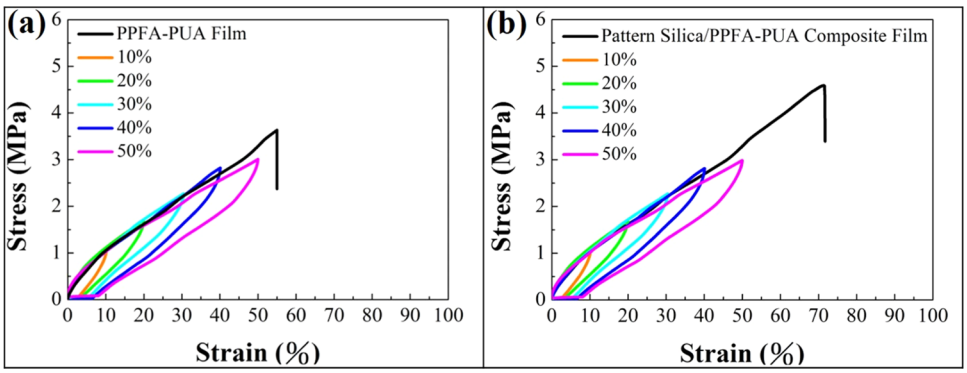

Figure 5. Cyclic tensile tests of (a) a PPFA-PUA film and (b) the riblet-like structure-covered silica hollow sphere colloidal crystal/PPFA-PUA composite film under different strains.

force for a few seconds, and then gradually recovers its original crystalline lattice. It is of great importance that the recovered reflection peak position matches well with the initial one (Figure S4), further demonstrating the restoration of the crystalline lattice. As would be expected, the reflection peak position can be reversibly switched for at least 25 cycles, while the corresponding structural color is turned between yellow and violet.

To comprehend the mechanochromic characteristics, normal-incidence reflection spectra of the silica hollow sphere colloidal crystal/PPFA-PUA composite film under varied uniaxial elongation ratios are collected using an ultraviolet−visible−near-infrared spectrometer and compared in Figure 4a. It is evident that the reflection peak position of the unstretched composite film locates at 580 nm (red curve), agreeing well with the theoretical one (581 nm, red arrow) calculated according to Bragg's law. This finding even verifies the hexagonal arrangement of doctor-blade-coated silica hollow sphere colloidal crystals. It is worth noting that the reflectance can be further improved though increasing the thickness of silica hollow sphere colloidal crystals.[48] Apparently, the reflection peak progressively blue-shifts while the composite film is stretched uniaxially. The peak position turns from 580 to 432 nm as the elongation ratio of the composite film reaches 50%. Interestingly, the peak position shift is in a nearly linear relationship with the elongation ratio (Figure 4b). The relationship can also be evaluated using the above-mentioned Bragg's equation

$$\lambda_{peak} = 2 \times (f_{air} \times n_{air}^2 + f_{silica} \times n_{silica}^2 + f_{PPFA\text{-}PUA} \times n_{PPFA\text{-}PUA}^2)^{1/2} \times d' \times \sin 90^\circ$$

where d' denotes the interlayer lattice spacing of the stretched composite film with an elongation ratio of ε (Figure S3). The f_{air}, f_{silica}, $f_{PPFA\text{-}PUA}$, n_{air}, n_{silica}, and $n_{PPFA\text{-}PUA}$ values are presumed to remain unchanged during the uniaxial stretching process, while d' can be expressed as follows.

$$\begin{aligned} d' &= (D^2 - a')^{1/2} \\ &= \left\{D^2 - \left[b'^2 + \left(\frac{(1+\varepsilon)D}{2}\right)^2\right]\right\}^{1/2} \\ &= \left\{D^2 - \left[b^2 + \left(\frac{(1+\varepsilon)D}{2}\right)^2\right]\right\}^{1/2} \\ &= \left\{D^2 - \left[\left(a^2 - \left(\frac{D}{2}\right)^2\right) + \left(\frac{(1+\varepsilon)D}{2}\right)^2\right]\right\}^{1/2} \\ &= \left\{D^2 - \left[\left(\left(\frac{2}{\sqrt{3}} \times \frac{D}{2}\right)^2 - \left(\frac{D}{2}\right)^2\right) + \left(\frac{(1+\varepsilon)D}{2}\right)^2\right]\right\}^{1/2} \\ &= \left\{\frac{11}{12}D^2 - \left(\frac{(1+\varepsilon)D}{2}\right)^2\right\}^{1/2} \\ &= \left\{\frac{11}{12} - \left(\frac{(1+\varepsilon)}{2}\right)^2\right\}^{1/2} \times D \end{aligned}$$

On account of that, the reflection peak position blue-shifts with the increase of elongation ratio. As disclosed in Figure 4b, the remarkable agreement between the calculated reflection peak positions and the measured ones under varied elongation ratios confirms the high crystalline quality of stretched colloidal crystals and the faithful mechanochromic tunability. It is worth mentioning that the introduction of larger silica hollow spheres generates a larger interlayer spacing. Consequently, it is valid to design and build a shark scale-patterned composite film with a tunable structural color across the entire visible spectrum.

The tensile behaviors of a PPFA-PUA film and a riblet-like structure-covered silica hollow sphere colloidal crystal/PPFA-PUA composite film are also evaluated in this study. It is evident that the PPFA-PUA film possesses a remarkable mechanical performance with a tensile strength of 3.6 MPa and a strain to failure of 54.9%, while the Young's modulus is estimated to be approximately 12.5 MPa (Figure 5a). In comparison with that, the introduction of silica hollow sphere-embedded surface patterns undoubtedly improves the mechanical properties in terms of permanent deformation and initial modulus. The stress−strain curve of the patterned composite film presents a tensile stress of 4.5 MPa, a tensile

https://doi.org/10.1021/acsami.3c03086
ACS Appl. Mater. Interfaces 2023, 15, 35311−35320

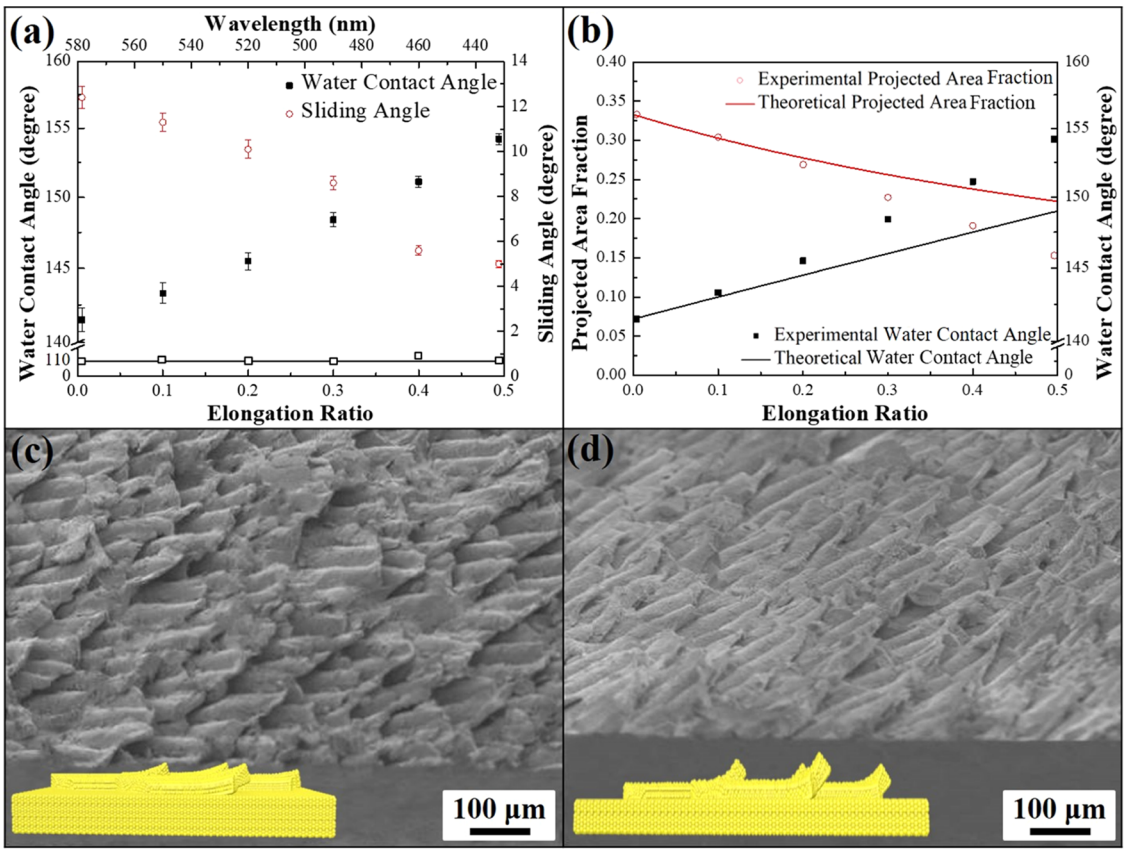

Figure 6. (a) Static water contact angles (black solid square) and sliding angles (red hollow circle) of a templated riblet-like structure-covered composite film with 280 nm hollow sphere colloidal crystals embedded under varied elongation ratios. The solid line indicates static water contact angles (black hollow square) of a featureless polymer film under varied elongation ratios. (b) Experimental and theoretical projected area fractions and static water contact angles of the specimen under varied elongation ratios. (c) Side-view SEM image of the specimen in an unstretched state. (d) Side-view SEM image of the specimen in a stretched state (elongation ratio = 0.5).

strain of 71.6%, and a Young's modulus of 13.4 MPa (Figure 5b). To better comprehend the elasticity of the materials, we perform cyclic tensile loading with a maximum strain of 10, 20, 30, 40, or 50%. Apparently, the hysteresis loop is enlarged as the strain increases from 10 to 50%, resulting from the stretch-induced dissociation of weak physical interactions between polymer chains. Moreover, most of the specimens exhibit negligible unrecoverable deformations, which further demonstrate their high elasticities.

Static water contact angles (SWCAs) on the shark scale-patterned silica hollow sphere colloidal crystal/PPFA-PUA composite film under varied elongation ratios are subsequently gauged using a drop-shape analyzer to assess their surface hydrophobicities (Figure S5). As shown in Figure 6a, the SWCAs stay almost the same (~110°, black hollow square) on a featureless PPFA-PUA film against stretching. By contrast, the SWCA on the unstretched shark scale-patterned composite film can achieve 141°, which is obviously larger than the ones either on a shark scale pattern-covered PPFA-PUA film (132°) or on a silica/PPFA-PUA composite film with silica hollow sphere colloidal crystals embedded (120°), respectively (Figures S6 and S7). It is believed that the combination of micrometer-scale patterns and nanometer-scale protuberances (Figure 2d–f) considerably reduces interactions with water droplets, thereby leading to a larger contact angle. The SWCA on the shark scale-patterned composite film is further increased upon longitudinal stretching (black solid square), and a contact angle of 154° is acquired as the elongation ratio of the composite film reaches 50%. Owing to the diminished interactions, nonwetting water droplets are apt to roll off the composite film and eliminate any contaminating substance at a low sliding angle, estimated by the difference between advancing and receding water contact angles. In comparison with the estimated sliding angles of the micrometer-scale pattern-covered substrate and the nanometer-scale protuberance-covered substrate, the shark scale-patterned composite film presents an even smaller sliding angle (Figures S8 and S9). This sliding angle exhibits an opposite tendency with respect to the elongation ratio (Figures S10 and S11), and a minimal sliding angle of 5° can be obtained (red hollow circle) (Figure 6a). Indeed, the surface hydrophobicity and self-cleaning capability of the shark scale-patterned composite film can be easily ameliorated through reducing its surface energy. The experimental observations on the incomplete wetting behaviors can be quantitatively described by adopting the Cassie–Baxter model[49]

$$\cos\theta_c = f \times \cos\theta - (1 - f)$$

where θ_c and θ stand for the SWCAs on structure-covered surfaces and featureless surfaces, respectively, while f denotes the solid projected area fraction. For the unstretched shark scale-patterned composite film, the original solid projected area fraction (f_o) is determined as a result of $\cos 141° = f_o \cos 110° - (1 - f_o)$. Upon stretching longitudinally, the shark scale pattern density is inversely proportional to the length of the

https://doi.org/10.1021/acsami.3c03086
ACS Appl. Mater. Interfaces 2023, 15, 35311–35320

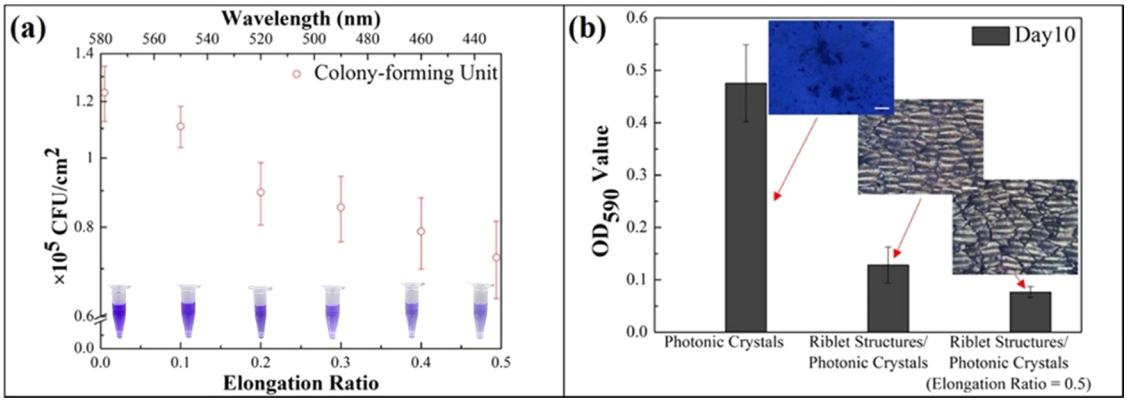

Figure 7. (a) Counts of the bacteria colony forming units on a templated riblet-like structure-covered composite film with 280 nm silica hollow sphere colloidal crystals embedded under varied elongation ratios. (b) Residual biofilms on a composite film with 280 nm silica hollow sphere colloidal crystals embedded, an unstretched templated riblet-like structure-covered composite film with 280 nm silica hollow sphere colloidal crystals embedded, and a stretched templated riblet-like structure-covered composite film with 280 nm silica hollow sphere colloidal crystals embedded (elongation ratio = 0.5). The scale bar represents 100 μm.

composite film, thereby f can be computed using a simple calculation as follows.

$$f = f_o \times \frac{1}{(1+\varepsilon)}$$

Afterward, the theoretically predicted SWCAs using the Cassie−Baxter equation are compared with the experimental ones in Figure 6b. It is found that the theoretical and experimental results display similar tendencies, though the experimental ones are slightly larger. This is reasonable as we assume the solid−water contact area and the length of film are directly proportional to the reciprocal of each other. In reality, the shark scale-patterned composite film subjected to a longitudinal extension in the direction of tensile force (Y direction) undergoes a lateral contraction in the transverse direction (Z direction) (Figure S3), which is known as the Poisson effect. Even though the shark scale patterns are not directly stretched by the tensile force, the foregoing contraction causes directionally structural deformations in the Z direction. As a result, the riblet-like structures tend to slant upward in the longitudinal stretching process (Figure 6c,d). The formation of upward-slanting structures generates even smaller solid projected area fractions (f) and thus brings about larger SWCAs and smaller sliding angles. This will move the theoretical curves closer to the experimental results. Importantly, it is evident that tunable superhydrophobic/self-cleaning surfaces with visual color responses can be achieved on the shark scale-patterned composite films. On the contrary, SWCAs (black solid square) and sliding angles (red hollow circle) of a silica colloidal crystal/PPFA-PUA composite film are independent of elongation ratios (Figure S12), though its color blue-shifts as the composite film is stretched uniaxially.

The integration of riblet-like structures and nanometer-scale protuberances can even act as an antifouling coating. To further evaluate its antifouling capability, short-term antibacterial and long-term anti-biofilm performances of the shark scale-patterned photonic crystals are challenged with *E. coli*. After spraying an *E. coli* suspension (~1×10^9 CFU/mL) onto the surfaces, the specimens are cultured for 24 h before determining the equivalent CFU. As would be expected, hydrophobic surfaces with greater SWCAs and smaller sliding angles are less favorable for bacterial attachments. In comparison with the 24 h bacterial attachment on an unpatterned composite film (~6×10^5 CFU/mL), the number of adherent bacteria on the shark scale-patterned composite film is greatly reduced to ~1×10^5 CFU/mL (Figure 7a). To put it simply, nearly 85% of bacteria are further removed from the patterned specimen. Most of the bacterial suspension rolls off the riblet-like structures, leading to the lowering of the bacterial contamination. Importantly, the short-term antibacterial characteristics can be easily enhanced through stretching the specimen. The bacterial contamination is even reduced by another 40% as the elongation ratio reaches 0.5. The residual bacteria generate extracellular polymeric substances that facilitate attachment and biofilm formation whereby the microorganisms irreversibly grow onto the surface. For the biofilm formation assessment, biofilm attached on the specimens as stated previously are incubated at a constant shaking frequency for 10 days and then stained with CV. As displayed in Figure 7b, the unpatterned composite film exhibits a uniform deep-blue color, which identifies the formation of dense biofilm. By contrast, only part of the shark scale-patterned composite film is tinted with blue color, while its optical density measured at a wavelength of 590 nm (OD_{590} value) is decreased greatly. It is evident that the large topography variation of micrometer-scale riblet-like structures provides a physical barrier that prevents bacterial clusters from expanding into large-area biofilms.[50] Importantly, the upward-slanting riblet-like structures on the stretched patterned composite film (elongation ratio = 0.5) create an even smaller friction drag to facilitate boundary layer flow over the structure surfaces, which further hinders the biofilm formation during the inoculation. The findings demonstrate that the antifouling capability, and the corresponding structural color of the shark scale-patterned photonic crystals can be adjusted through longitudinally stretching the composite film.

CONCLUSIONS

By drawing inspiration from shark scales, a roll-to-roll compatible self-assembly technology is developed to engineer riblet-like structure-covered photonic crystals, the hexagonally close-packed silica hollow spheres of which are embedded in a PPFA-PUA copolymer matrix. The combination of micrometer-scale riblet-like structures and nanometer-scale protuberances demonstrates an elegant design to reduce interaction with water droplets and facilitate boundary layer flow over the

https://doi.org/10.1021/acsami.3c03086
ACS Appl. Mater. Interfaces 2023, 15, 35311−35320

structures. Upon stretching longitudinally, the temporarily deformed structures bring about different surface hydrophobicities, self-cleaning properties, and antifouling capabilities under varied elongation ratios. In addition, the reduced lattice spacing of the embedded colloidal crystals allows a remarkable color change with high color saturation. Such tunable superhydrophobic/antifouling structures with a visual color response will ultimately contribute to the next generation of biomedical, industrial, and environmental biotechnology applications.

■ ASSOCIATED CONTENT

Supporting Information

The Supporting Information is available free of charge at https://pubs.acs.org/doi/10.1021/acsami.3c03086.

SEM images and TEM images of silica hollow spheres; photographic images and SEM images of a PDMS negative replica; schematic illustration of a stretching shark scale-patterned composite film; optical reflection peak positions of the shark scale-patterned composite film switched between the stretching state and the released state; and static water contact angles, advancing water contact angles, receding water contact angles, and sliding angles of a featureless polymer film, a shark scale pattern-covered polymer film, a silica hollow sphere colloidal crystal-embedded composite film, and a shark scale pattern-covered composite film with silica hollow sphere colloidal crystals embedded under varied elongation ratios (PDF)

■ AUTHOR INFORMATION

Corresponding Authors

Hsiu-Wen Chien − *Department of Chemical and Materials Engineering, National Kaohsiung University of Science and Technology, Kaohsiung 82444, Taiwan;* orcid.org/0000-0001-5596-6281; Email: hsiu-wen.chien@nkust.edu.tw

Hongta Yang − *Department of Chemical Engineering, National Chung Hsing University, Taichung City 402202, Taiwan;* orcid.org/0000-0002-5822-1469; Email: hyang@dragon.nchu.edu.tw

Authors

Liang-Cheng Pan − *Department of Chemical Engineering, National Chung Hsing University, Taichung City 402202, Taiwan*

Shang-Yu Hsieh − *Department of Chemical Engineering, National Chung Hsing University, Taichung City 402202, Taiwan*

Wei-Cheng Chen − *Department of Chemical and Materials Engineering, National Kaohsiung University of Science and Technology, Kaohsiung 82444, Taiwan*

Fang-Tzu Lin − *Department of Chemical Engineering, National Chung Hsing University, Taichung City 402202, Taiwan*

Chieh-Hsuan Lu − *Department of Chemical Engineering, National Chung Hsing University, Taichung City 402202, Taiwan*

Ya-Lien Cheng − *Department of Chemical Engineering, National Chung Hsing University, Taichung City 402202, Taiwan*

Complete contact information is available at: https://pubs.acs.org/10.1021/acsami.3c03086

Author Contributions

[§]L.-C.P. and S.-Y.H. contributed equally to this work.

Notes

The authors declare no competing financial interest.

■ ACKNOWLEDGMENTS

This work was financially supported by the National Science Council (MOST 110-2221-E-005-050-MY2 and MOST 111-2221-E-005-010). The authors acknowledge the Instrument Center of National Chung Hsing University for the technical supports with a field emission scanning electron microscope.

■ REFERENCES

(1) Chaudhary, R.; Nawaz, K.; Khan, A. K.; Hano, C.; Abbasi, B. H.; Anjum, S. An Overview of the Algae-Mediated Biosynthesis of Nanoparticles and Their Biomedical Applications. *Biomolecules* **2020**, *10*, No. 1498.

(2) Liu, Q.; Ren, J. Y.; Lu, Y. S.; Zhang, X. L.; Roddick, F. A.; Fan, L. H.; Wang, Y. F.; Yu, H. R.; Yao, P. A Review of the Current In-Situ Fouling Control Strategies in MBR Biological Versus Physicochemical. *J. Ind. Eng. Chem.* **2021**, *98*, 42−59.

(3) Selim, M. S.; Yang, H.; Wang, F. Q.; Fatthallah, N. A.; Li, X.; Li, Y.; Huang, Y. Superhydrophobic Silicone/Sic Nanowire Composite as a Fouling Release Coating Material. *J. Coat. Technol. Res.* **2019**, *16*, 1165−1180.

(4) Peigneguy, F.; Cougnon, C.; Barry-Martinet, R.; Bressy, C.; Gohier, F. Antifouling Activities of Immobilized Ferrocenyl Glucose on a Glassy Carbon Surface. *ACS Appl. Mater. Interfaces* **2020**, *12*, 33370−33376.

(5) Rajala, P.; Bomberg, M.; Huttunen-Saarivirta, E.; Priha, O.; Tausa, M.; Carpen, L. Influence of Chlorination and Choice of Materials on Fouling in Cooling Water System under Brackish Seawater Conditions. *Materials* **2016**, *9*, No. 475.

(6) Gahlawat, G.; Choudhury, A. R. A Review on the Biosynthesis of Metal and Metal Salt Nanoparticles by Microbes. *RSC Adv.* **2019**, *9*, 12944−12967.

(7) Pandin, C.; Coq, Le; Deschamps, D.; Vedie, J.; Rousseau, R.; Aymerich, T.; Briandet, S. R. Complete Genome Sequence of Bacillus Velezensis QST713: A Biocontrol Agent that Protects Agaricus Bisporus Crops against the Green mould Disease. *J. Biotechnol.* **2018**, *278*, 10−19.

(8) Amara, I.; Miled, W.; Ben Slama, R.; Ladhari, N. Antifouling Processes and Toxicity Effects of Antifouling Paints on Marine Environment. A review. *Regul. Toxicol. Pharmacol.* **2018**, *57*, 115−130.

(9) Kong, X. W.; Zhu, C. X.; Lv, J.; Zhang, J.; Feng, J. Robust Fluorine-Free Superhydrophobic Coating on Polyester Fabrics by Spraying Commercial Adhesive and Hydrophobic Fumed SiO_2 Nanoparticles. *Prog. Org. Coat.* **2020**, *138*, No. 105342.

(10) Li, R. J.; Li, J. Y.; Rao, L. H.; Lin, H. J.; Shen, L. G.; Xu, Y. C.; Chen, J. R.; Liao, B. Q. Inkjet Printing of Dopamine Followed by UV Light Irradiation to Modify Mussel-Inspired PVDF Membrane for Efficient Oil-Water Separation. *J. Membr. Sci.* **2021**, *619*, No. 118790.

(11) Norfarhana, A. S.; Ilyas, R. A.; Ngadi, N. A Review of Nanocellulose Adsorptive Membrane as Multifunctional Wastewater Treatment. *Carbohydr. Polym.* **2022**, *291*, No. 119563.

(12) Menon, D. M. N.; Pugliese, D.; Janner, D. Infrared Nanosecond Laser Texturing of Cu-Doped Bioresorbable Calcium Phosphate Glasses. *Appl. Sci.* **2022**, *12*, No. 3516.

(13) Ma, R. H.; Lu, X. L.; Zhang, S. Z.; Ren, K.; Gu, J.; Liu, C.; Liu, Z. Q.; Wang, H. L. Constructing Discontinuous Silicon-Island Structure with Low Surface Energy Based on the Responsiveness of Hydrophilic Layers to Improve the Anti-Fouling Property of Membranes. *J. Membr. Sci.* **2022**, *659*, No. 120770.

(14) Faÿ, F.; Gouessan, M.; Linossier, I.; Rehel, K. Additives for Efficient Biodegradable Antifouling Paints. *Int. J. Mol. Sci.* **2019**, *20*, No. 361.

(15) Kim, S.; Ye, S. H.; Adamo, A.; Orizondo, R. A.; Jo, J.; Cho, S. K.; Wagner, W. R. A Biostable, Anti-Fouling Zwitterionic Polyurethane-Urea Based on PDMS for Use in Blood-Contacting Medical Devices. *J. Mater. Chem. B* **2020**, *8*, 8305−8314.
(16) Ni, X. X.; Gao, Y. J.; Zhang, X. H.; Lei, Y.; Sun, G.; You, B. An Eco-Friendly Smart Self-Healing Coating with NIR and Ph Dual-Responsive Superhydrophobic Properties Based on Biomimetic Stimuli-Responsive Mesoporous Polydopamine Microspheres. *Chem. Eng. J.* **2021**, *406*, No. 126725.
(17) Liu, Y.; Li, G. L.; Han, Q.; Lin, H. B.; Li, Q.; Deng, G.; Liu, F. Construction of Electro-Neutral Surface on Dialysis Membrane for Improved Toxin Clearance and Anti-Coagulation/Inflammation through Saltwater Fish Inspired Trimethylamine N-Oxide (TMAO). *J. Membr. Sci.* **2022**, *641*, No. 119900.
(18) Xiao, S. N.; Hao, X. Q.; Yang, Y. F.; Li, L.; He, N.; Li, H. L. Feasible Fabrication of a Wear-Resistant Hydrophobic Surface. *Appl. Surf. Sci.* **2019**, *463*, 923−930.
(19) Parimelazhagan, V.; Jeppu, G.; Rampal, N. Continuous Fixed-Bed Column Studies on Congo Red Dye Adsorption-Desorption Using Free and Immobilized *Nelumbo Nucifera* Leaf Adsorbent. *Polymers* **2022**, *14*, No. 54.
(20) Xiao, X.; Zhang, C. H.; Ma, H. Y.; Zhang, Y. H.; Liu, G. L.; Cao, M. Y.; Yu, C. M.; Jiang, L. Bioinspired Slippery Cone for Controllable Manipulation of Gas Bubbles in Low-Surface-Tension Environment. *ACS Nano* **2019**, *13*, 4083−4090.
(21) Shirtcliffe, N.; McHale, G.; Newton, M. Learning from superhydrophobic plants: The Use of Hydrophilic Areas on Superhydrophobic Surfaces for Droplet Control. *Langmuir* **2009**, *25*, 14121−14128.
(22) Lai, C.-J.; Chen, Y. J.; Wu, M. X.; Wu, C. C.; Tang, N. T.; Hsu, T. F.; Lin, S. H.; Li, H. F.; Yang, H. T. Self-Cleaning and Anti-Fogging Hierarchical Structure Arrays Inspired by Termite Wing. *Appl. Surf. Sci.* **2023**, *616*, No. 156484.
(23) Han, Z. W.; Wang, Z.; Li, B.; Feng, X. M.; Jiao, Z. B.; Zhang, J. Q.; Zhao, J.; Niu, S. C.; Ren, L. Q. Flexible Self-Cleaning Broadband Antireflective Film Inspired by the Transparent Cicada Wings. *ACS Appl. Mater. Interfaces* **2019**, *11*, 17019−17027.
(24) Wang, Y. K.; Liu, Y. P.; Li, J.; Chen, L. W.; Huang, S. L.; Tian, X. L. Fast Self-Healing Superhydrophobic Surfaces Enabled by Biomimetic Wax Regeneration. *Chem. Eng. J.* **2020**, *390*, No. 124311.
(25) Jo, W.; Kang, H. S.; Choi, J.; Jung, J.; Hyun, J.; Kwon, J.; Kim, I.; Lee, H.; Kim, H. T. Light-Designed Shark Skin-Mimetic Surfaces. *Nano Lett.* **2021**, *21*, 5500−5507.
(26) Dai, W.; Alkahtani, M.; Hemmer, P. R.; Liang, H. Drag-Reduction of 3D Printed Shark-Skin-Like Surfaces. *Friction* **2019**, *7*, 603−612.
(27) Gabler-Smith, M. K.; Lauder, G. V. Ridges and Riblets: Shark Skin Surfaces Versus Biomimetic Models. *Front. Mar. Sci.* **2022**, *9*, No. 81.
(28) Li, X. M.; Deng, J. X.; Yue, H. Z.; Ge, D. L.; Zou, X. Q. Wear Performance of Electrohydrodynamically Atomized WS2 Coatings Deposited on Biomimetic Shark-Skin Textured Surfaces. *Tribol. Int.* **2019**, *134*, 240−251.
(29) Zhang, Q. Y.; Bai, X. H.; Li, Y.; Zhang, X. F.; Tian, D. L.; Jiang, L. Ultrastable Super-Hydrophobic Surface with an Ordered Scaly Structure for Decompression and Guiding Liquid Manipulation. *ACS Nano* **2022**, *16*, 16843−16852.
(30) Chien, H. W.; Chen, X. Y.; Tsai, W. P.; Lee, M. Inhibition of Biofilm Formation by Rough Shark Skin-Patterned Surfaces. *Colloids Surf. B* **2020**, *186*, No. 110738.
(31) Liu, Y.; Gu, H. M.; Jia, Y.; Liu, J.; Zhang, H.; Wang, R. M.; Zhang, B. L.; Zhang, H. P.; Zhang, Q. Y. Design and Preparation of Biomimetic Polydimethylsiloxane (PDMS) Films with Superhydrophobic, Self-Healing and Drag Reduction Properties via Replication of Shark Skin and SI-ATRP. *Chem. Eng. J.* **2019**, *356*, 318−328.
(32) Fathi, F.; Rashidi, M. R.; Pakchin, P. S.; Ahmadi-Kandjani, S.; Nikniazi, A. Photonic Crystal Based Biosensors: Emerging Inverse Opals for Biomarker Detection. *Talanta* **2021**, *221*, No. 121615.
(33) Cai, G. Y.; Liu, F. L.; Wu, T. Z. Slippery Liquid-Infused Porous Surfaces with Inclined Microstructures to Enhance Durable Anti-Biofouling Performances. *Colloids Surf. B* **2021**, *202*, No. 111667.
(34) Gou, T.; Liu, T.; Su, Y.; Li, J.; Guo, Y.; Huang, J.; Zhang, H.; Li, Y.; Zhang, Z.; Ma, Y.; Zhang, Z.; Gao, X. Bio-Inspired Inclined Nanohair Arrays with Tunable Mechanical Properties for Effective Directional Condensed Microdroplets Self-Jumping. *Chem. Eng. J.* **2022**, *427*, No. 130887.
(35) Li, W. Y.; Wang, Y.; Li, M.; Garbarini, L. P.; Omenetto, F. G. Inkjet Printing of Patterned, Multispectral, and Biocompatible Photonic Crystals. *Adv. Mater.* **2019**, *31*, No. 1901036.
(36) Li, M. M.; Lyu, Q.; Peng, B. L.; Chen, X. D.; Zhang, L. B.; Zhu, J. T. Bioinspired Colloidal Photonic Composites: Fabrications and Emerging Applications. *Adv. Mater.* **2022**, *34*, No. 2110488.
(37) Li, Z. W.; Fan, Q. S.; Yin, Y. D. Colloidal Self-Assembly Approaches to Smart Nanostructured Materials. *Chem. Rev.* **2022**, *122*, 4976−5067.
(38) Deng, R. H.; Xu, J. P.; Yi, G. R.; Kim, J. W.; Zhu, J. T. Responsive Colloidal Polymer Particles with Ordered Mesostructures. *Adv. Funct. Mater.* **2021**, *31*, No. 2008169.
(39) Zhang, Z. J.; Qi, Y.; Ma, W.; Zhang, S. F. Wettability-Controlled Directional Actuating Strategy Based on Bilayer Photonic Crystals. *ACS Appl. Mater. Interfaces* **2021**, *13*, 2007−2017.
(40) Wang, K.; Li, C.; Li, Z.; Li, H.; Li, A.; Li, K.; Lai, X.; Liao, Q.; Xie, F.; Li, M.; Song, Y. A Facile Fabrication Strategy for Anisotropic Photonic Crystals Using Deformable Spherical Nanoparticles. *Nanoscale* **2019**, *11*, 14147−14154.
(41) Li, P. X.; Wang, Z.; Ma, K.; Chen, Y.; Yan, Z. F.; Penfold, J.; Thomas, R. K.; Campana, M.; Webster, J. R. P.; Washington, A. Multivalent Electrolyte Induced Surface Ordering and Solution Self-Assembly in Anionic Surfactant Mixtures: Sodium Dodecyl Sulfate and Sodium Diethylene Glycol Monododecyl Sulfate. *J. Colloid Interface Sci.* **2020**, *565*, 567−581.
(42) Yin, L.; Tian, Q.; Boyjoo, Y.; Hou, G. J.; Shi, X.; Liu, J. Synthesis of Colloidal Mesoporous Silica Spheres with Large Through-Holes on the Shell. *Langmuir* **2020**, *36*, 6984−6993.
(43) Yang, Q. S.; Li, L.; Zhao, F.; Wang, Y. W.; Ye, Z. S.; Hua, C.; Liu, Z. Y.; Bohinc, K.; Guo, X. H. Spherical Polyelectrolyte Brushes as Templates to Prepare Hollow Silica Spheres Encapsulating Metal Nanoparticles. *Nanomaterials* **2020**, *10*, No. 799.
(44) Chai, Z. M.; Childress, A.; Busnaina, A. A. Directed Assembly of Nanomaterials for Making Nanoscale Devices and Structures: Mechanisms and Applications. *ACS Nano* **2022**, *16*, 17641−17686.
(45) Liu, F. F.; Zhang, S. F.; Jin, X.; Wang, W. T.; Tang, B. T. Thermal-Responsive Photonic Crystal with Function of Color Switch Based on Thermochromic System. *ACS Appl. Mater. Interfaces* **2019**, *11*, 39125−39131.
(46) Zhou, C. T.; Qi, Y.; Zhang, S. F.; Niu, W. B.; Wu, S. L.; Ma, W.; Tang, B. T. Bilayer Heterostructure Photonic Crystal Composed of Hollow Silica and Silica Sphere Arrays for Information Encryption. *Langmuir* **2020**, *36*, 1379−1385.
(47) Kim, J. H.; Hong, S. H.; Seong, K. D.; Seo, S. Fabrication of Organic Thin-Film Transistors on ThreeDimensional Substrates Using Free-Standing Polymeric Masks Based on Soft Lithography. *Adv. Funct. Mater.* **2014**, *24*, 2404−2408.
(48) Li, T.; Liu, G. J.; Kong, H.; Yang, G. Z.; Wei, G.; Zhou, X. Recent Advances in Photonic Crystal-Based Sensors. *Coord. Chem. Rev.* **2023**, *475*, No. 214909.
(49) Tang, L.; Zeng, Z. X.; Wang, G.; Shen, L. L.; Zhu, L. J.; Zhang, Y. X.; Xue, Q. J. Study of Oil Dewetting Ability of Superhydrophilic and Underwater Superoleophobic Surfaces from Air to Water for High-Effective Self-Cleaning Surface Designing. *ACS Appl. Mater. Interfaces* **2019**, *11*, 18865−18875.
(50) Rostami, S.; Tekkesin, A. I.; Ercan, U. K.; Garipcan, B. Biomimetic Sharkskin Surfaces with Antibacterial, Cytocompatible, and Drug Delivery Properties. *Biomater. Adv.* **2022**, *134*, No. 112565.

https://doi.org/10.1021/acsami.3c03086
ACS Appl. Mater. Interfaces 2023, 15, 35311−35320